Lowering thermal conductivity in thermoelectric $Ti_{2-x}NiCoSnSb$ half Heusler high entropy alloys

#Soumya Ranjan Mishra[1,2], #Anirudha Karati[3,4], Sanyukta Ghosh[5],
Ramesh Chandra Mallik[5], Rajashekhara Shabadi[6], P S Sankara Rama Krishnan[2],
Satyesh Kumar Yadav[1], R.V. Ramanujan[2], B.S. Murty[1,7,*]

[1]*Department of Metallurgical and Materials Engineering, Indian Institute of Technology Madras, Chennai, India.*
[2]*School of Materials Science and Engineering, Nanyang Technological University, Singapore*
[3]*Department of Chemistry, Indian Institute of Technology Madras, Chennai, India.*
[4]*International Advanced Research Centre for Powder Metallurgy & New Materials (ARCI), PO Balapur, Hyderabad, India.*
[5]*Thermoelectric Materials and Devices Laboratory, Department of Physics, Indian Institute of Science, Bengaluru (Bangalore), India.*
[6]*Univ. Lille, CNRS, INRAE, Centrale Lille, UMR 8207 - UMET - Unité Matériaux et Transformations, F-59000 Lille, France.*
[7]*Department of Metallurgical and Materials Engineering, Indian Institute of Technology Hyderabad, Kandi, India.*

ABSTRACT

$Ti_{2-x}NiCoSnSb$ (x = 0.125, 0.250, 0.375, and 0.500) half Heusler (HH) high entropy thermoelectric alloys were synthesized by the arc melting (VAM) – ball milling (BM) – spark plasma sintering (SPS) route. The impact of secondary phase content on the thermoelectric properties in these alloys was examined. Ni-rich intermetallic (Ni_3Sn_2, Ni_3Sn_4) compounds were observed; the intermetallic content increased for lower Ti content, e.g., $Ti_{1.5}NiCoSnSb$. A Ni-rich full Heusler (FH) secondary phase was also observed. These results were consistent with first-principles calculations that show that the formation enthalpy of $Ti_{1.5}NiCoSnSb$ was higher than that of $Ti_2NiCoSnSb$ and the full Heusler (FH) $TiNi_2Sn$ phase. In lower Ti content samples, the electrical conductivity increased, and lattice thermal conductivity decreased at the expense of thermopower owing to higher FH and the Ni_3Sn_2 phase content. $Ti_{1.5}NiCoSnSb$ exhibited lower lattice thermal conductivity of 3.5 W/mK, compared to 5.4 W/mK at 823 K for $Ti_2NiCoSnSb$ due to increased phonon scattering at HH/Ni_3Sn_2 interfaces. But considering the decreasing power factor with lower Ti content, the maximum ZT obtained in $Ti_{1.875}NiCoSnSb$

(0.171 at 973 K) was only marginally higher than the value for $Ti_2NiCoSnSb$. Further, compositional tuning is hence necessary to maximize the power factor.

Keywords: Full-Heusler, Half-Heusler, High entropy alloy, Thermoelectric.

*** Corresponding Author**, Email: bsm@iith.ac.in murty@iitm.ac.in

[#]**These authors have contributed equally to the manuscript.**

Graphical abstract:

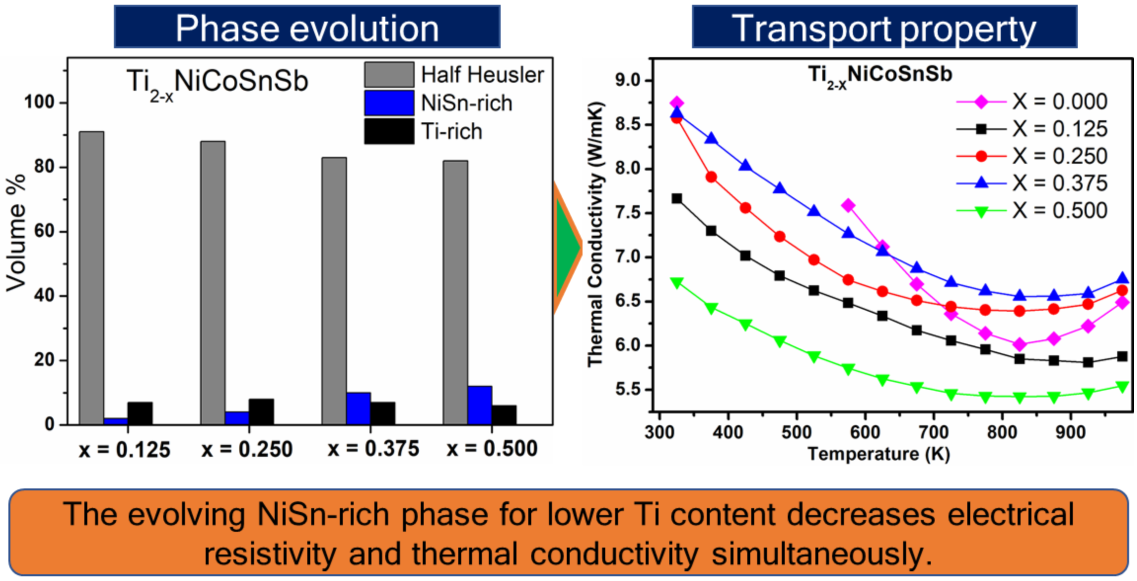

The evolving NiSn-rich phase for lower Ti content decreases electrical resistivity and thermal conductivity simultaneously.

1. Introduction

Due to the depletion of natural reserves and an impending energy crisis, there is an urgent need for energy conservation and recycling. The conversion of waste energy to electricity makes thermoelectric effect-based energy recovery and recycling an extremely attractive and viable technology. Since the discoveries of the Seebeck and Peltier effects in the early 19th century [1], several efforts have been made to enhance thermoelectric (TE) efficiency. Thermoelectricity today finds diverse applications in microelectronics [2], as TE generators in hybrid cars, as Peltier refrigerators and heaters, and in space applications [3, 4]. Solar and Photo TE applications have also been ongoing research topics [5, 6]. The efficiency of TE devices (η) is a product of their Carnot efficiency ($\Delta T/T_h$), which primarily depends on the system design and the figure of merit (ZT) which characterizes the constituent TE material [7]. ZT depends on both electrical (Seebeck coefficient (S), electrical conductivity (σ)) and thermal (thermal conductivity (κ)) parameters [2] and is given by:

$$ZT = \frac{S^2\sigma}{\kappa} \tag{i}$$

Thermoelectric alloy composition selection has been based on Ioffe's findings [8] on the optimized concentration needed to obtain the maximum power factor ($S^2\sigma$). The total thermal conductivity (κ) is due to the collisions of free electrons in the crystal (κ_e) and the effect of phonons resulting from the vibrations of the crystal lattice (κ_l). The electronic component κ_e depends directly on σ, the lattice phononic component κ_l is determined by the complexity of the crystal structure and tunable microstructural features. Presently, the materials employed for high temperature thermoelectricity include oxides, SiGe, and half Heusler (HH) alloys [9, 10]. However, the high contact resistance of the oxides [11] and the high cost of SiGe [9] hinder their applications. Hence, HH are attractive candidates for such applications [12, 13].

Heusler alloys with the Co_2MnSi type structure, are composed of four FCC lattices at 0 0 0 (4a), ¼ ¼ ¼ (4b), ½ ½ ½ (4c), and ¾ ¾ ¾ (4d), adopting the $Fm\bar{3}m$ (225) space group. The half-Heusler counterparts have the 4d Wyckoff position vacant and adopt the $F\bar{4}3m$ space group, as in the MgAgAs structure. HH alloys with a total valence electron count (VEC) of 18 are semiconducting and find applications as TE materials. HH alloys possess a high-power factor (~ up to 6 mW/mK^2) due to their narrow band gap, are composed of earth abundant elements, and do not need toxic or radioactive precursors. Their machinability, low contact resistance with metallic contacts and low thermal fatigue makes them attractive for high temperature TE generators [7, 14]. However, they possess a *relatively higher κ value* ranging from 1.8 to 20 W/mK [15, 16].

These alloys are generally synthesized by melting routes [17], solid-state synthesis (SSS) [18], or mechanical alloying (MA) [19], with the crushed or milled powders being subsequently compacted through hot isostatic pressing (HIP) or spark plasma sintering (SPS) under vacuum [18]. Generally, a single-phase material is not obtained and long annealing times are often required. However, the resulting grain growth, structural disorder and compositional changes are detrimental to the TE transport properties [20, 21]. Chen *et al.* have shown that the *ex-situ* dispersion of nanocrystalline zirconia (9 vol %) in Hf and Pd doped ZrNiSn lowers κ and enhances ZT by 1.35 times to 0.75 [22]. Similarly, Makongo *et al.*, have shown that precipitation of the nano full-Heusler (FH) phase in $Zr_{0.25}Hf_{0.75}Ni_{1+x}Sn_{0.975}Bi_{0.025}$, enhances electrical transport properties *via* effective carrier filtering, while simultaneously lowering κ_l [23]. Isovalent heavy atom doping can promote mass scattering to lower κ, with a ZT of 0.94 obtained in Ta and Hf-doped ZrNiSn at 923K [24].

High entropy alloys (HEAs) are considered prospective TE materials owing to the lower κ_l value observed due to phonon scattering by the distorted lattice. These single-phase materials with high crystal symmetry possess a high power factor [25]. Ren *et al.* suggested crystallographic design through aliovalent substitution to form double, triple, or quadruple HH. A double HH is formed by combining two 18 electron HH or a 17 and 19 electron HH alloys in such a way that the overall VEC is a multiple of 18. Similarly, in triple HH, three HH phases combine to give a VEC which is a multiple of 18. With the increasing number of atoms in the crystal, the crystal complexity escalates, the order-disorder transitions helps lower κ_l further at higher temperatures[26]. In such alloy systems, phase separation can also contribute to the lowering of κ_l [27]. High entropy has been realized in HH alloys by adding multiple elements to lower κ, which is called entropy engineering. For instance, entropy engineering in NbCoSb by equimolar additions of Hf, Zr, Ta, V, and Ti, resulted in a ZT of 0.31 at 923K [15].

Karati *et al.* synthesized double HH $Ti_2NiCoSnSb$ and demonstrated a lower κ_l owing to high entropy effect and HH/HH phase separation [28, 29], and a simultaneous increase in S and σ due to charge carrier filtering. Additionally, unlike in the case of TiNiSn or TiCoSb, no additional annealing was required in this entropy stabilized alloy[28]. Park *et al.* found that annealing of sintered MNiSn (M=Ti, Zr, Hf) drastically reduced σ and increased κ, resulting in a lower ZT [21]. This necessitates a lower annealing time in HH alloys.

First-principles calculations further revealed the impact of phase separation in $Ti_2NiCoSnSb$ on its thermal properties [29]. However, the presence of TiC impurities lowers the overall power factor in $Ti_2NiCoSnSb$ [30]. While lowering of Ti content to increase phase purity has not been studied in TiNiSn, in HH NbCoSn, lower Nb decreased the NbSn type intermetallic and FH phase fraction [31]. To enhance phase purity of the HH phase in NbCoSn, excess Co was added, or Nb content was decreased to lower the FH phase fraction [32]. Ferluccio *et al.* showed that κ_l reaches as low as 4 W/mK at an optimum Nb content of 0.94 atomic fraction [32]. In $Nb_{1-x}CoSb$, κ is significantly lowered. Due to the lower metallic Nb_5Sb_4 secondary phase content, the thermopower is also enhanced, leading to a *ZT* of 0.9 at 1123K for $Nb_{0.83}CoSb$ [33]. Similar results have been observed by lowering V and Ta content in 19 electron n-type $V_{1-x}CoSb$ and $Ta_{1-x}CoSb$ [34]. Recently, the combined effect of simultaneously lowering Nb and Sb content in NbCoSb on their TE properties was investigated [35]. And the optimum level of FH phase content in $TiNi_{1+x}Sn$ improved TE properties [36].

To increase the phase purity, lower Ti content was investigated in this present study. With lower Ti content, in the case of the formation of the single HH phase, the VEC would decrease leading to an apparent p-type doping that would influence the electrical transport properties. Hence, in this present study, we report the electrical and thermal transport properties of the $Ti_{2-x}NiCoSnSb$ set of alloys where x = 0.125 (VEC = 17.75), 0.25 (VEC = 17.5), 0.375 (VEC = 17.25) and 0.5 (VEC = 17) and they were compared with the $Ti_2NiCoSnSb$ (x = 0.000) sample. However, for lower Ti content, an increase in Ni_3Sn_2 second phase content significantly influences the transport properties in these alloys. Based on the effect of the processing routes analyzed in $Ti_2NiCoSnSb$, the arc melting followed by 1h ball milling, and sintering (VAM-1hBM-SPS) route with the highest ZT was chosen for synthesizing these alloys. And though mechanical alloying under argon led to close ZT values, owing to the chances of additional contamination like WC pickup from the vials, above method was preferred.

2. Materials and methods

For synthesizing the $Ti_{2-x}NiCoSnSb$ (x = 0.125, 0.250, 0.375, and 0.500) set of alloys, elemental granules of Ti and Sn, and chunks of Ni, Co, and Sb (all 99.5% pure) obtained from Loba Chemie were utilized. The elements were taken in stoichiometric proportion (with 5% excess Sb to compensate for vaporization losses) for vacuum arc melting (VAM) in a Vacuum Technology arc melting unit. To reduce losses due to evaporation, elemental Sn and Sb were first alloyed, followed by melting with high melting point Ti, Ni, and Co [28]. Finally, these master alloys were arc melted by placing the higher melting master alloy on top to form the VAM alloy. A Ti getter was used to minimize oxidation.

The VAM alloys were crushed and milled in a Fritsch Pulverisette P-5 high energy planetary ball mill. 1 hour milling was done at 300 rpm under acetone media using Tungsten carbide (WC) vials and 10 mm WC balls. The obtained powders were then consolidated in a Dr. Sinter SPS-650 Spark plasma sintering unit of Sumitomo Metals, Japan in 20 mm graphite dies at 1273 K, with the temperature applied in 10 min and held for 5 min. 50 MPa pressure was applied within 3 min from the start of the sintering process and maintained throughout the process. Final pellets obtained were 3-3.5 mm thick.

About 500 μm was scraped off from both sides of the compacted samples. The samples were resized for TE property measurements using a Struers Minitom low-speed IsoMet. The electrical properties (S and σ) were measured by the differential and four-probe method, respectively. The Linseis LSR-3 system for S and σ measurement was used in the temperature range of 300 K to 973 K using samples resized to dimensions of 12 × 2 × 2 mm^3. To obtain thermal conductivity (κ), the thermal diffusivity (α) was measured using a laser heating source and IR detector in a Netzsch LFA-427 setup.

The density of the samples was measured using Archimedes setup with the weight of the samples measured in air and water (Table S1 of the Supporting information). Theoretical density was calculated using the rule of mixtures of the known phases found from SEM (summation of the phase fraction and density of respective phase). The samples were resized to dimensions of 10 × 10 × 2 mm^3 for laser flash measurements. The electronic thermal conductivity (κ_e) dependence on electrical conductivity is given by the Wiedemann-Franz law as $\kappa_e = LT\sigma$. The Lorentz number (L) at a given temperature was determined from the equivalent S values using the single parabolic band (SPB) model, which estimates the reduction of chemical potential due to phonon scattering [37].

The crystallography of the phases and their evolution in these alloys were determined utilizing an X'Pert Pro mpd powder X-Ray diffractometer, which is equipped with a copper-Kα radiation source (wavelength of 0.15406 nm). The XRD pattern was fitted with a Pseudo-Voight function to analyze the phase and crystallite size and strain. A polycrystalline silicon standard was used to subtract instrumental broadening effects. A high-intensity micro-XRD (RINT RAPID-II by Rigaku Corporation, Japan) was used to characterize the minority phases in the sample.

The microstructural evaluation was evaluated by a Helios G4 UX DualBeam microscope (FESEM) unit manufactured by Thermo Fisher Scientific FEI Company. A Bruker-Quantax energy-dispersive X-ray spectroscopy (EDS) unit attached to the FESEM was used for elemental analysis of the phases and compositional mapping. In the focused ion beam (FIB) unit attached to a Carl-Zeiss-cross beam 540, a gallium ion beam was employed to thin down cross-sectional transmission electron microscopy samples to ~70 nm. Scanning

/Transmission electron microscopy (STEM/TEM) studies were conducted using a spherical aberration corrected JEM ARM200F (JEOL corporation, Japan) microscope operated at 200 kV. STEM-EDS mapping was performed using the Oxford SDD STEM-EDS detector.

Density functional theory (DFT) based analysis with similar parameters for the x = 0.000 sample [29] was used for first-principles calculations in the x = 0.500 sample with 8 vacancy sites in the 96-atom supercell simulated from Monte Carlo calculations in alloy theoretic automated toolkit (ATAT) [38]. For DFT calculations Vienna Ab initio Simulation Package (VASP) was employed, and a generalized gradient type (GGA) pseudopotential (for inner shell electrons) was used for local approximation along with 2×2×2 K-point grid generated using Monkhorst-Pack calculations [39, 40]. Structural relaxation was carried out with cut-off energy and ionic displacement levels of 10^{-5} eV and 10^{-2} eV/Å, respectively.

3. Results and discussion

3.1. Crystal structure and Phase evolution:

3.1.1. Vacuum arc melting

In the VAM samples, a small tin and full Heusler (FH) phase content could be observed in the X-ray diffractograms (Figure 1(a)). These samples are denoted as x = 0.125 ($Ti_{1.875}NiCoSnSb$), x = 0.250 ($Ti_{1.75}NiCoSnSb$), x = 0.375 ($Ti_{1.625}NiCoSnSb$), and x = 0.500 ($Ti_{1.5}NiCoSnSb$), respectively, where x denotes the difference between the Ti content in the sample and that in $Ti_2NiCoSnSb$. $Ti_2NiCoSnSb$ shall be denoted as x = 0.000. In the case of formation of the pure HH phase, the occupancy of Ti in its lattice site would decrease from 1.00 in the x = 0.000 sample to 0.75 in the x = 0.500 sample, correspondingly the valence electrons count (VEC) would decrease from 18 in the x = 0.000 sample to 17 in the x = 0.500 sample.

The BSE micrographs in Figure 3 show that the white Sn-rich phase and whitish-grey phase content increased from ~3.8 vol % in the x = 0.125 sample (3(a)), to ~6.7 vol% in the x = 0.250 sample (3(b)), to ~ 12.1 vol % in the x = 0.375 sample (3(c)) and decreased slightly to ~11.5 vol % in the x = 0.500 sample (3(d)), as can be seen from the phase analysis in Table S2 of the Supporting information. The whitish-grey phase was found to be NiSn-rich in Table S2 of the Supporting information. Due to its low phase fraction, it was not observed in the XRD results.

In the VAM samples, the dark grey phase had ~ 45 % Ni and Co (Table S2 of the Supporting information), indicating the presence of the full Heusler (FH) phase. Precipitation of a secondary FH phase of the Ni_2TiSn type in the half Heusler (HH) matrix of the NiTiSn type was greater in the sintered alloys as compared to VAM samples, as is evident from the X-ray diffractograms in Figure 1(a) and 1(c). Hazama *et al.* [41] suggested that Ni and Sn were expelled from the compound during SPS. It was found that the excess Ni had occupied the empty tetrahedral vacancies (interstices) of HH TiNiSn to form the Ni-rich FH phase. Surprisingly, the FH phase was observed in the sub-stoichiometric Ti samples, with the expected lowering of VEC. The FH phase fraction marginally decreased with lower Ti content in these samples [Figure 1(c)]. The composition analysis (Table S2 of the Supporting information) revealed the HH phase to be TiCoSb rich and the FH phase to be Ni_2TiSn rich, indicative of phase separation in these alloys.

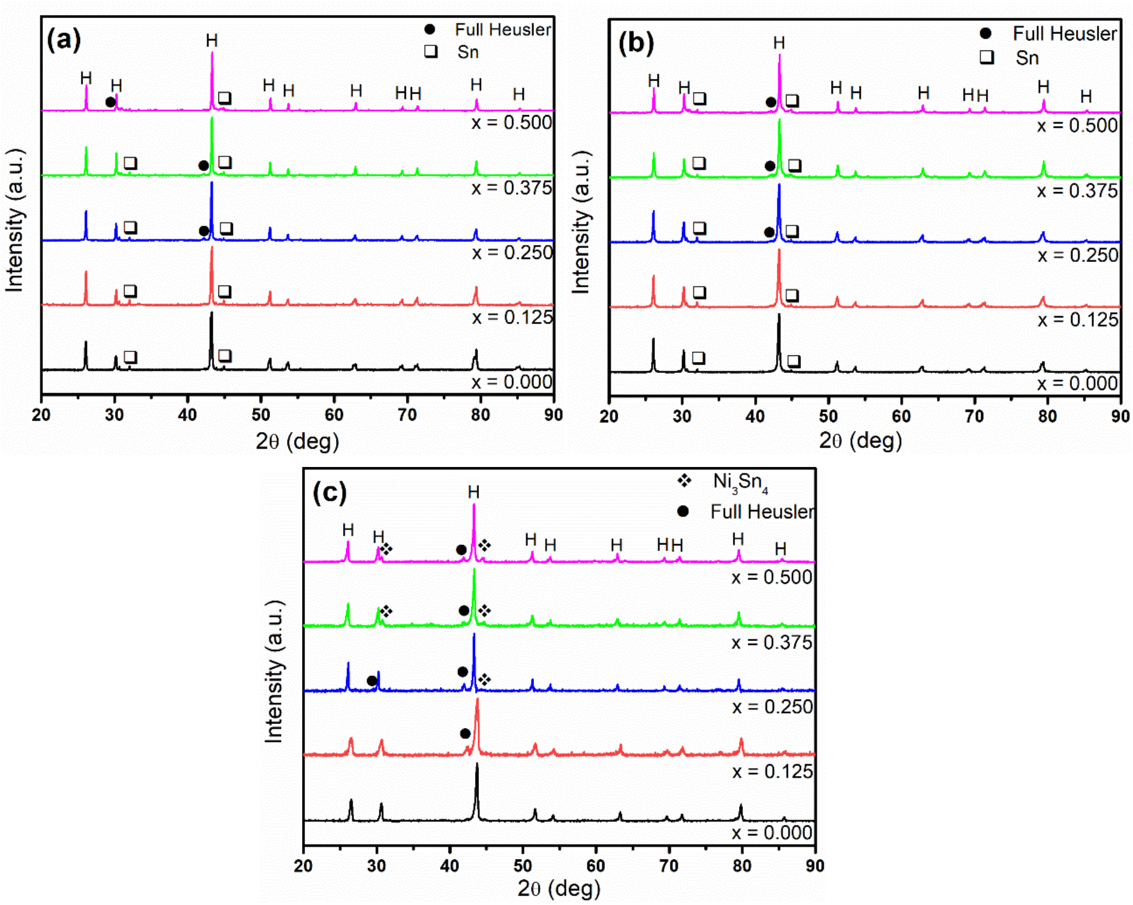

Fig. 1. X-Ray Diffractograms of (a) vacuum arc melted, (b) 1h ball milled and (c) spark plasma sintered $Ti_{2-x}NiCoSnSb$ (x = 0.125, 0.250, 0.375, 0.500) samples and a comparison with $Ti_2NiCoSnSb$ (reported in [28]). In all the diffractograms H denotes the half Heusler phase.

3.1.2. *Ball milling and spark plasma sintered samples*

Almost no change was observed after 1h milling (Figure 1(b)). In the sintered samples, the x = 0.125 sample revealed only the FH secondary phase, as can be seen in the high intensity

XRD diffractogram in Figure 2, the XRD pattern in Figure 1(c), and the BSE micrograph in Figure 4a. Considering the difficulty in clearly discerning the minority phases in normal XRD, high intensity XRD was performed. The black Ti-rich phase observed in the x = 0.000 sample was also seen in these samples [28]. The FH phase is expected to be present when VEC is greater than 18 in HH alloys. But here, even with VEC decreasing from 18 to 17, the FH phase was observed by XRD; with decreasing VEC, there is a marginal decrease in FH phase content.

The NiSn-rich phase increased for lower Ti content owing to the reduced availability of Ti to form the HH matrix phase. The low melting point tin present in the VAM samples (Figure 1(a)) started to dissolve into the matrix during ball milling (Figure 1(b)) and intermetallic Ni_3Sn_4 and Ni_3Sn_2 phases were observed after sintering (Figure 2, Figure 1(c)).

In the x = 0.000 sample, no Co based intermetallics were observed, as was the case in samples with up to 25% lower Ti content (x = 0.500 sample). The NiSn-rich phase can be seen in the high intensity XRD pattern in Figure 2, with a zoomed view revealing a NiSn-rich intermetallic as inset of Figure 2. From the high intensity XRD pattern, it is observed that with decreasing Ti fraction from x = 0.125 to x = 0.500 samples, the FH phase fraction marginally decreased while the metallic Ni_3Sn_4 phase content increased.

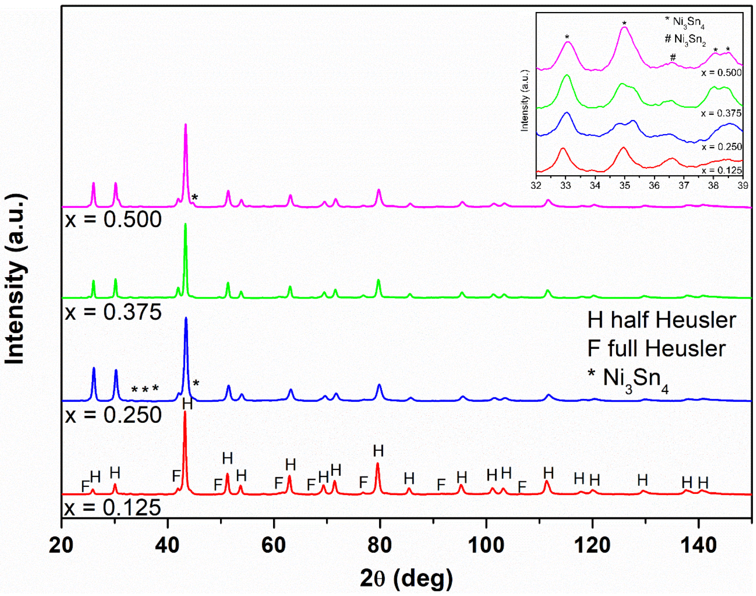

Fig. 2. High intensity X-ray diffractograms revealing phase evolution in sintered $Ti_{2-x}NiCoSnSb$ (Minority NiSn phase shown in insets). Here in the Diffractogram H denotes the half Heusler phase and F the full Heusler phase.

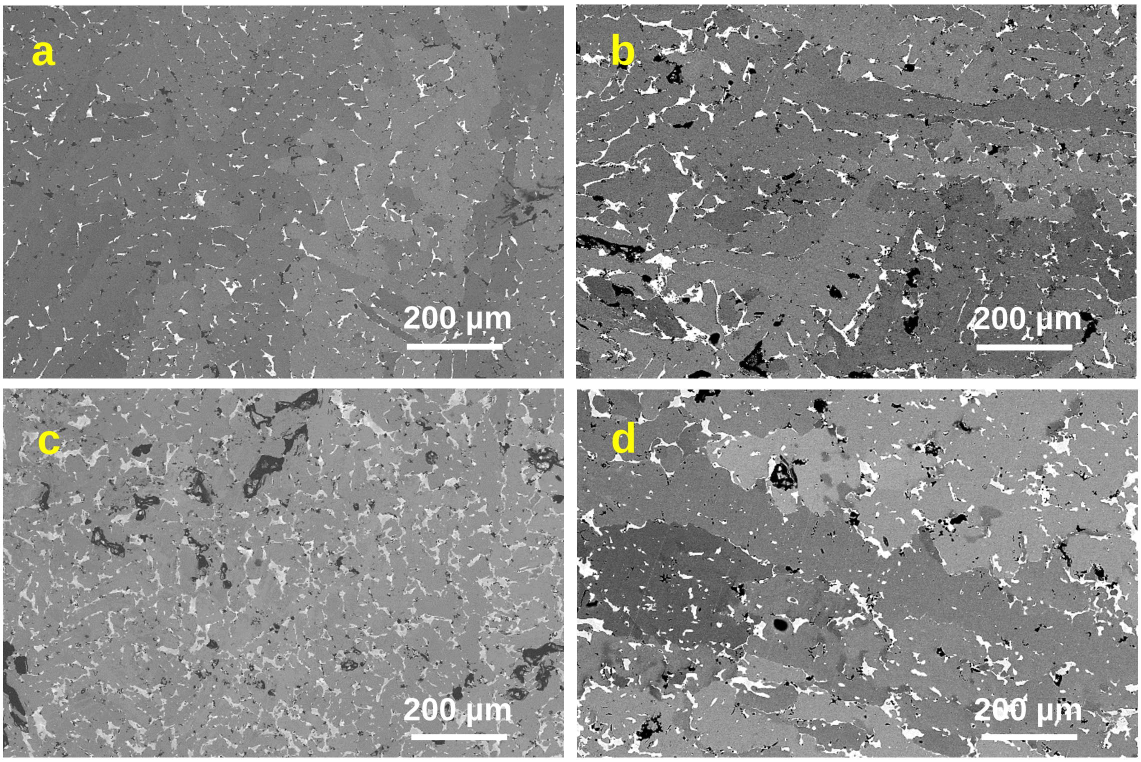

Fig. 3. BSE micrographs showing 4 phases (grey, dark grey, black and white) in vacuum arc melted (a) x = 0.125, (b) x = 0.250, (c) x = 0.375 and (d) x = 0.500 samples

This is evident from the increase in the volume fraction of the white phase with a NiSn-rich composition, from 0.02 in the x = 0.125 sample (Figure 4a) to 0.04 in the x = 0.250 sample (Figure 4b) to 0.10 in the x = 0.375 sample (Figure 4c) to 0.12 in the x = 0.500 sample (Figure 4d), as seen in the BSE imaging results. This trend is also evident from the phase and composition analysis in Figure 6 and Table S3 of the Supporting information. Therefore, further tuning of Ti content may yield a composition between x = 0.125 and x = 0.250 sample with the minimum amount of FH and NiSn rich phase, yielding the double HH of TiNiSn and TiCoSb with the desired highest HH phase fraction.

Small pockets of dark Ti-rich (oxycarbide) phases were seen in $Ti_2NiCoSnSb$ [28]. White NiSn-rich phases could be seen in the EDS elemental mapping of the x = 0.375 sample in Figure 5. A black phase, comprising Ti oxycarbides as well as porosities, was found to be ~8 volume % in all the alloys (Figure 6d, Table S3 of the Supporting information). However, it is difficult to accurately separate the Ti oxycarbide phase from the porosity. In the x = 0.125 and x = 0.250 samples, the black phase surrounded the white phase; however, the black phase was seen inside the white phase in the x = 0.375 and x = 0.500 samples.

The occurrence of the TiCoSb-rich grey phase and the TiNiSn-rich dark grey phase in these samples could be indicative of phase separation between the two HH components of the double HH. However, compared to the x = 0.000 sample, the dark grey phase fraction was lower in the x = 0.125 sample (~ 0.03) and not clearly discernible in the other compositions, owing to increased HH/Ni_3Sn_4 phase separation. Due to its lower phase fraction and small size, the FH phase was not visible in these samples. In the high-intensity XRD, the FH phase is discernible; it is difficult to separate the grey and dark grey phases in the SEM micrographs of the sintered samples. The overall equation pertaining to the mechanochemical reaction in these alloys can be given as:

$$Ti_2NiCoSnSb + yO_2 + zC - xTi \rightarrow (TiNiSn + TiCoSb) + Ni_2TiSn + Ni_3Sn_2 + TiO_yC_z \qquad \text{(ii)}$$

The Ni_3Sn_2 phase content increased with larger x, O_2 was picked up during melting, and C was picked up from the graphite dies during sintering. The matrix was TiCoSb-rich, while the FH phase was Ni_2TiSn-rich. Considering that the Ti-Ni-Co-Sn-Sb quinary system is constituted of 10 binary (Ti-Ni, Ti-Co, …) phase systems [42], the above phase separation could be attributed to the low solubility of Ni-Sn near equilibrium with Ti-Co exhibiting extended solubility near equilibrium and Ti-Ni and Ti-Sn forming line compounds at equilibrium. Hence, on deviating from the stochiometric Ti content, Ni_3Sn_2, and FH phases were observed.

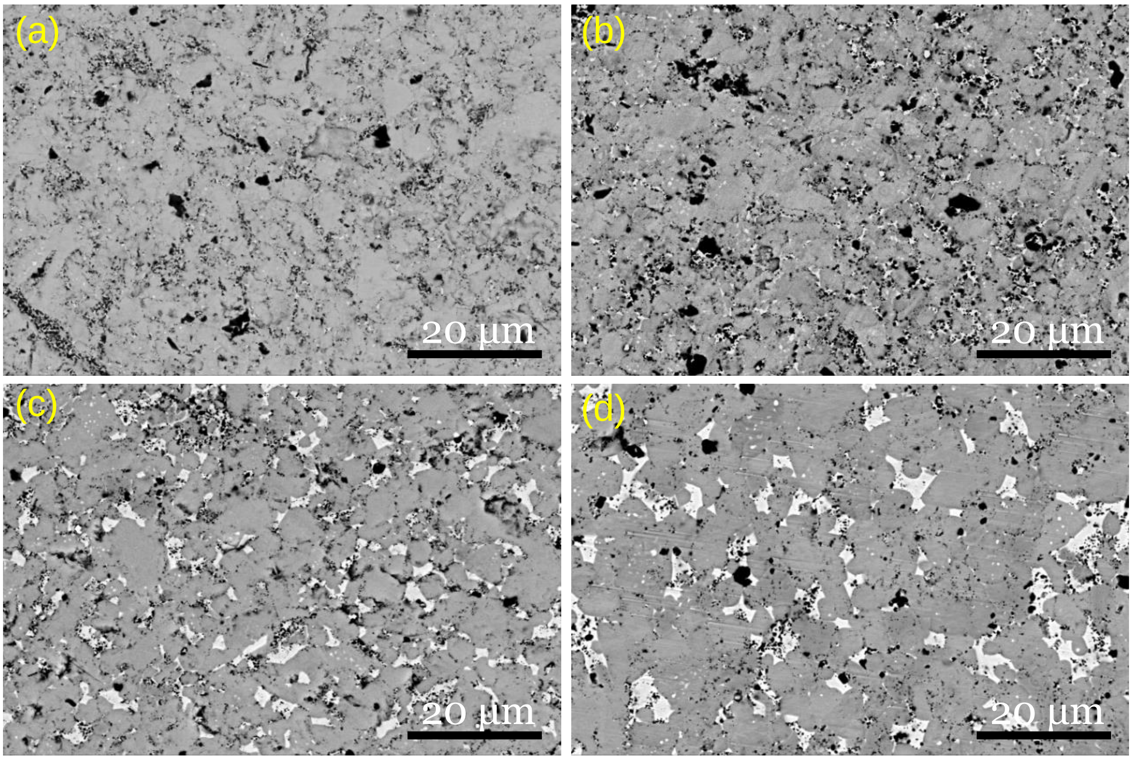

Fig. 4. BSE Micrographs depicting 3 phases in 1h ball milled and spark plasma sintered $Ti_{2-x}NiCoSnSb$ (x = 0.125 (a), 0.25 (b), 0.375 (c) and 0.5 (d) respectively).

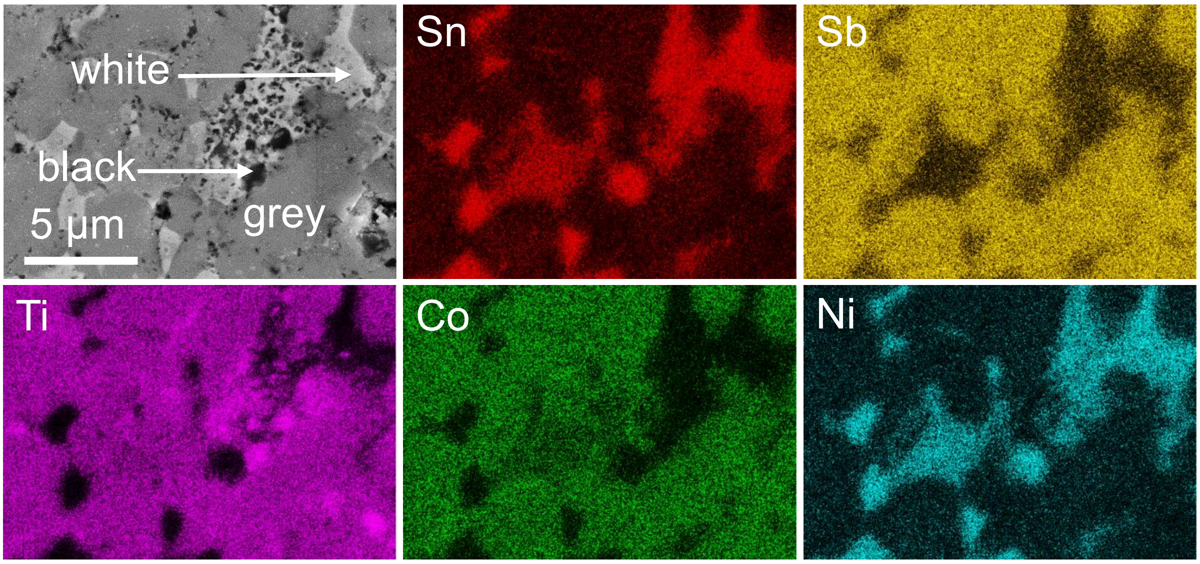

Fig. 5. EDS Mapping showing 3 (TiCoSb rich grey, Ni-Sn rich White and Ti-rich Black) phases in $Ti_{1.625}$NiCoSnSb (x = 0.375) alloy.

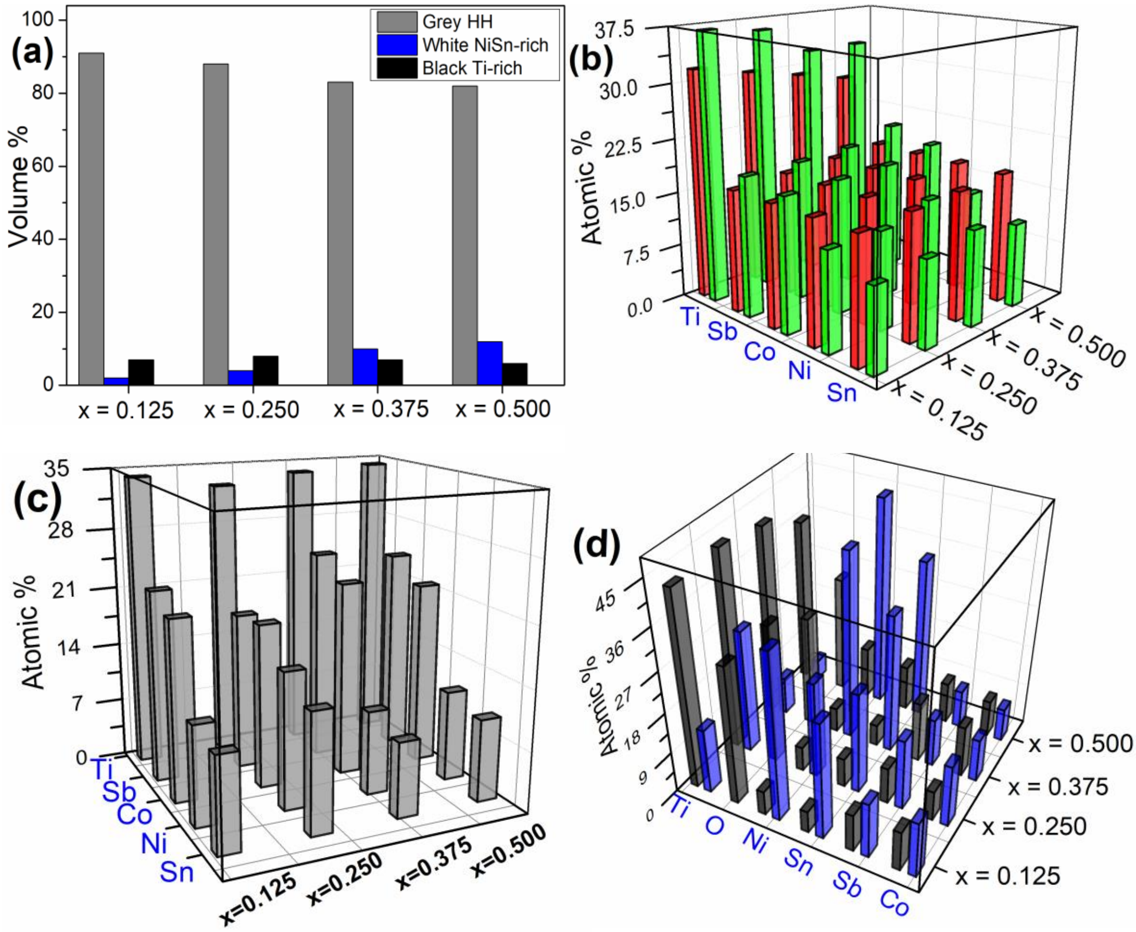

Fig. 6. (a) Volumetric phase analysis of Ti_{2-x}NiCoSnSb (x = 0.125, 0.250, 0.375, and 0.500) samples, comparative analysis of their (b) Overall (green) and Nominal (red) composition, (c) Grey phase, and (d) black (black) and white (blue) phase compositions.

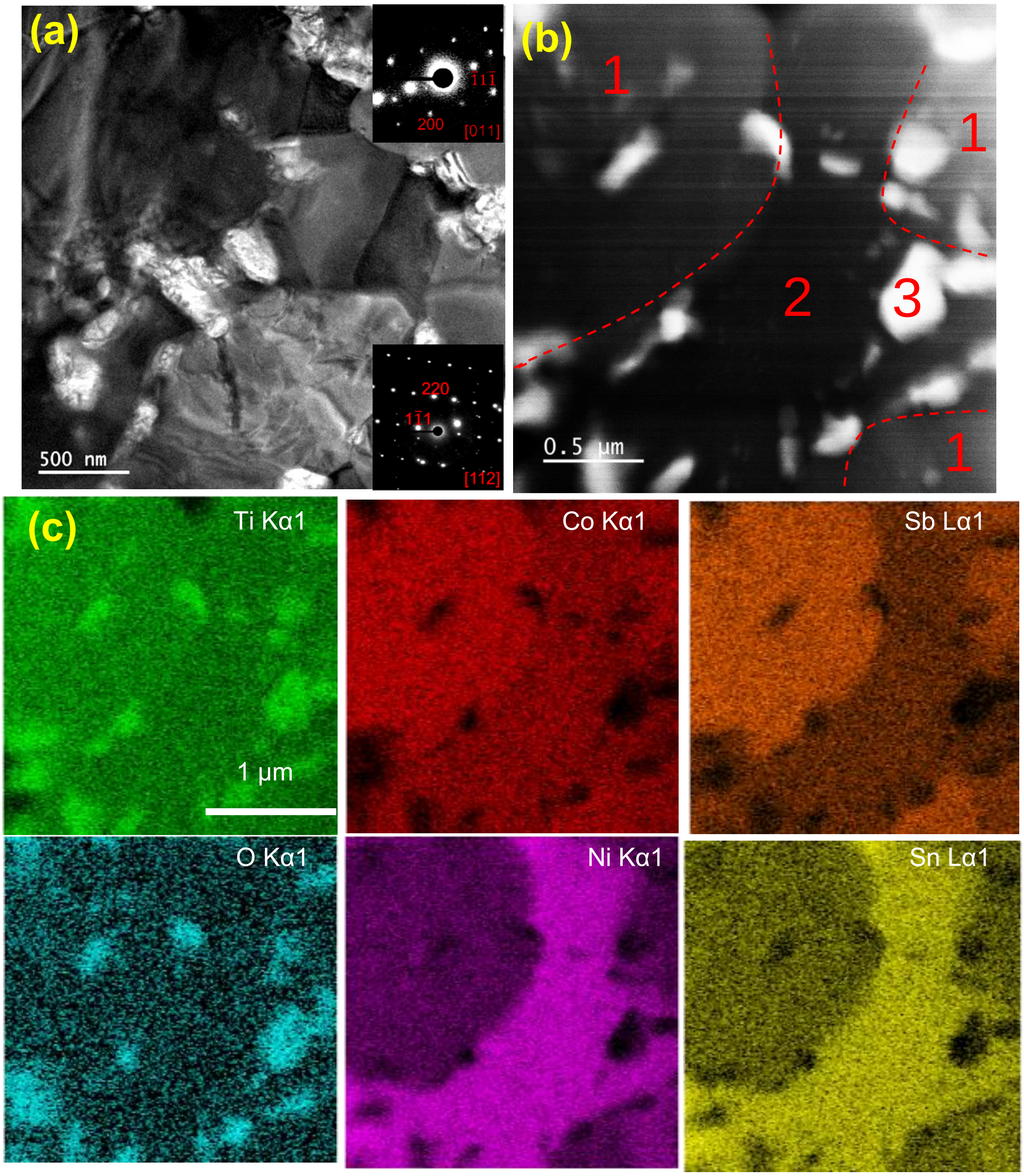

Fig. 7. (a) Bright field micrograph with Ni_3Sn_2 orthorhombic SADP and HH FCC SADP inset, (b) bright field STEM micrograph of $Ti_{1.625}NiCoSnSb$, and (c) STEM EDS mapping of the corresponding region (in b) depicting HH phase (1), Ni_3Sn_2 phase (2) and TiO_2 particles (3) in the phase boundary.

The bright field TEM images in Figure 7a exhibited three types of contrast: grey, black and bright white. The STEM EDS mapping shown in Figure 7c correspond to the STEM bright field image Figure 7b. Point EDS in Table S4 of the Supporting information revealed that the bright white particles were titania, the grey phase is the HH phase which is TiCoSb rich. The black phase is NiSn rich with a relatively low Ti content. The black phase with ~25% Ti, ~50% Ni+Co and ~25% Sn+Sb is indicative of the presence of the Full Heusler phase.

The SADP analysis revealed the grey phase to possess an FCC crystal symmetry as in the case of HH alloys (Figure 7a inset), while the black phase revealed the orthorhombic crystal structure of Ni_3Sn_2, as shown in the inset of Figure 7a. As was observed in the SEM results, the titania particles appear to be pinning the HH/Ni_3Sn_2 phase boundaries. The Ni_3Sn_2 phase of ~1 micron size was distributed uniformly in the matrix.

3.2. Thermoelectric properties and microstructural correlation:

3.2.1. Electrical transport properties:

In these double HH samples, with decreasing Ti content, the valence electron count (VEC), assuming a single HH phase ought to drop from 18 to 17 for the double HH phase and display p-type doping. Interestingly, all the samples exhibited negative S values, signifying n-type behavior [28]. Compositional analysis in Table S3 (Supporting information) reveals that even though the HH content decreased with lower Ti content, the amount of Ti in the HH phase remains almost constant. This and the zero-peak shift in the HH Phase observed in Figure 2 indicate that no p-type doping has occurred. *Instead, all the samples are n-type semiconductors with the metallic phase increasing for lower Ti content.* Furthermore, the Ti-rich phase in the x = 0.000 sample was also present in the samples with lower Ti content, and the semiconducting HH (grey) phase content diminished with lower Ti content. So, enhancement of the HH phase purity of the x = 0.000 sample by lowering the Ti content to increase the *S* value was not realized.

With declining semiconducting phase content, the *S* values decreased for lower Ti content samples (Figure 8a). The *S* value reached as high as 118 µV/K at 873 K in the x = 0.125 sample, which is marginally lower than that of 127 µV/K in the x = 0.000 sample at 873 K [28]. The maximum *S* value decreased systematically to 112, 98, and 84 µV/K for the x = 0.250, x = 0.375, and x = 0.500 samples, respectively.

With decreasing Ti content from the x = 0.000 sample to x = 0.500 sample, apart from a decrease in the semiconducting (grey HH-rich) phase content, an increase in the metallic (white NiSn-rich) phase content was also observed (Figure 6a). Hence, the electrical conductivity followed an inverse trend as that of the *S* values and increased from the x = 0.000 sample to the x = 0.500 sample (Figure 8b). A 33.8% decrease in S values and an 48.2% increase in electrical conductivity were observed with lowering Ti content from the x = 0.000 sample [28] to the x = 0.500 sample. For accurate analysis of the results, an average of 3 readings for each transport property was taken at each temperature. The mean data with error margins for the electrical resistivity and thermopower is given in Figure S2 of the supporting information.

In the higher Ti content (x = 0.000, 0.125, and 0.250) samples, at ~870 K, the *S* values saturated, possibly due to the electron filling of the conduction band [28]. This effect has been reported to be due to the bipolar effect. Due to the increase in minority charge carrier (here holes) concentration, there is no appreciable change in the *S* values. In HH systems, there are a few reports of a transition from a semiconducting to a metallic state [43] but the Goldsmid-Sharp band gap, calculated from the saturated *S* value by the equation $E_g = 2e|S|_{max}T_{max}$, does not support this possibility [44]. For instance, in the x = 0.250 sample, the calculated Goldsmid-Sharp band gap of 0.19 eV indicates a narrow band semiconductor and is suggestive of the bipolar effect. But, surprisingly, in the x = 0.375 and x = 0.500 samples, the *S* values didn't saturate and were found to be increasing at 973 K. The saturation of the S values due to the electron filling of the conduction band has been observed at around 600 K in pristine TiCoSb [45]. Since the TiCoSb-rich semiconducting HH phase decreased for lower Ti content, the saturation of the *S* values in the lower Ti content samples might occur at higher temperatures.

While thermopower does not show an appreciable change due to the bipolar effect, a change in the slope of the electrical conductivity indicates the bipolar effect. In all the samples, the electrical conductivity increased and then decreased, indicating a transition from an n-type semiconducting to a p-type semiconducting state and an increase in minority (hole) carrier concentration [32]. The critical temperature associated with activation of minority carriers increased for lower Ti content. Figure 8b shows that electrical conductivity decreased beyond 473 K for the x = 0.125 and x = 0.250 samples, while electrical conductivity decreased beyond 523 K for the x = 0.375 sample and beyond 623 K for the x = 0.500 sample. This effect can be associated with an increasing metallic character (increase in Ni-rich metallic phase content) of the samples with decreasing Ti content, which inversely affects the onset of minority charge carriers (holes) activation [32, 46]. Due to the increasing metallic behavior, the maximum electrical conductivity increased from 0.81×10^5 S/m at 473 K in the x = 0.125 sample to a maximum electrical conductivity of 1.17×10^5 S/m at 623 K in the x = 0.500 sample (Figure 8b).

The S^2 values decreased by 79% from the x = 0.000 sample to the x = 0.500 sample, while electrical conductivity increased by 48.2 % from the x = 0.000 sample to the x = 0.500 sample (Figure 8a and 8b). Since the power factor depends on the square of the *S* values and only linearly on the electrical conductivity values, the power factor decreased systematically from the x = 0.000 sample to the x = 0.500 sample. And owing to this the bipolar transition observed in the electrical conductivity was not observed in the power factor. Instead, the power factor seemed to saturate around 873 K in higher Ti content (x = 0.000, 0.125, and 0.250) samples and was increasing even at 973 K for lower Ti content samples. Thus, the power factor follows a similar dependency upon temperature as the *S* values. A power factor of 1.02 W/mmK^2 was obtained at 873 K in the x = 0.125 sample, compared to 1.11 W/mmK^2 in the case of the x = 0.000 sample (Figure 8c). The maximum power factor decreased to 0.90 W/mmK^2 at 923 K for the x = 0.250 sample, to 0.88 W/mmK^2 at 973 K for the x = 0.375 sample, and to 0.77 W/mmK^2 at 973 K for the x = 0.500 sample. The inverse relation between the Ni_3Sn_2 second phase volume and power factor at 50 and 873 K is evident from Figure 9a.

3.2.2. Lowering of thermal conductivity and analyzing the figure of merit:

It has been observed in the case of metallic FH phase precipitation in $TiNi_{1+x}Sn$ alloys that both the metallicity of the second phase and the interfacial scattering of phonons at the FH/HH phase interface affects the thermal conductivity [36, 46]. At an optimum level of FH phase precipitation, the effect of the metallicity of the second phase starts to overcome the effect of interfacial scattering, and the lowest possible thermal conductivity (κ) and lattice thermal conductivity (κ_l) values are obtained at that point.

In the alloys studied here, owing to phase separation, the grey HH phase was found to be TiCoSb rich. The Ni_2TiSn type FH phase was found in the x = 0.125 and x = 0.250 samples, though the FH phase fraction decreased in the x = 0.375 and x = 0.500 samples (Figures 2 and 6). The Ti-rich oxycarbide phase did not show appreciable change in volume fraction compared to the $Ti_2NiCoSnSb$ (x = 0.000) sample [28]. The NiSn-rich phase content increased from the x = 0.000 to the x = 0.500 sample, leading to a lowering of power factor, as seen in metallic samples. At the same time, it led to lower κ through interfacial scattering.

In these alloys, phonon scattering can happen at the HH/FH interface or HH/Ni_3Sn_2 interface, or at grain boundaries. Even the fine nanosized black Titanium oxycarbide phase can preferentially scatter phonons. The metallicity of the decreasing FH phase and increasing Ni_3Sn_2 intermetallic phase for lower Ti content also impacts the thermal conductivity in these samples. The combination of NiSn-rich phases and the FH phase in the x = 0.125 sample led to lower κ_l (~ 4.5 W/mK at 923 K) through phonon scattering (Figure 8e). Lower lattice thermal conductivity due to phonon scattering at the FH/HH interface in TiNiSn has been observed by Douglas *et al* [36]. The black sub-micron-sized Ti-rich phase inside and around the Ni_3Sn_2 phase forms additional interfaces for phonon scattering. The effect of scattering by the nanosized black phase has also been shown by Karati *et al.* in double HH $Ti_2NiCoSnSb$ and $Ti_2FeNiSb_2$ [28, 47].

The trade-off between increasing secondary phase size (increase in interfacial area) and metallicity with lower Ti content led to the x = 0.250 and x = 0.375 sample having relatively similar κ and κ_l values as the x = 0.000 sample. The large (~ 7 µm) Ni_3Sn_2 phase in the x = 0.500 sample led to much lower κ_l (~ 3.3 W/mK) (Figure 8e) and κ (5.4 W/mK) values (Figure 8d) as compared to the x = 0.000 sample (~ 4.95 W/mK, ~ 6.3 W/mK, respectively) at 923 K due to enhanced phonon scattering. The κ value was lower than that of the parent HH alloys TiNiSn (6.3 W/mK) and TiCoSb (9.1 W/mK) at 873 K too [16, 36]. Ferluccio *et al.* showed that Nb depletion in NbCoSb was equally efficient in lowering κ compared to alloying or substitution of heavier elements [32]. In the present study, *a 17% reduction in* κ *(x = 0.500 sample) through the lowering of Ti content in the samples* is consistent with the results of Ferluccio *et al.* κ_l and κ hence followed a parabolic trend with respect to lowering of Ti content (Figure 8e and 9b).

κ_e (Figure 8e), on the other hand, varied with compositions similar to the electrical conductivity trends. In all the samples, κ_e was found to be increasing for higher temperatures. A closer look at Figure 8e revealed that the rate of increase of κ_e was larger for lower Ti content in these samples which is in accordance with the electrical conductivity trends. All the samples displayed Umklapp scattering with decreasing κ_l with temperature. The rate of decrease of κ_l was lower between 673 K to 973 K in samples with lower Ti content. This was observed because, owing to phonon-phonon scattering, κ_l varies as 1/T with increasing temperature (Umklapp scattering) leading to saturation of κ_l values at higher temperatures. Similar saturation of κ_l at high temperatures has been observed in $MFe_{1-x}Co_xSb$ HH alloys [15] too. Since the κ values are a combination of the κ_l and κ_e values, from Figure 8d, the κ value can be seen to increase after 873 K in all the samples. This sort of *booster bipolar effect* has been observed in the thermal transport properties of NbCoSb [35] and in $MFe_{1-x}Co_xSb$ HH alloys [15]. This effect could be due to the enhanced κ value of the metallic phases at higher temperatures overcoming the phonon scattering occurring due to interfacial scattering. It other words, a combination of increasing κ_e values and almost constant κ_l values with higher temperatures led to increasing κ values at higher temperatures. Hence, while all the samples have lower κ values than the x = 0.000 sample at lower temperatures, at elevated temperatures (beyond 673 K), the x = 0.000 sample has lower κ and κ_l than the x = 0.250 and x = 0.375 samples. This is evident from the variation of thermal conductivity at 323 and 873 K with composition in Figure 9b.

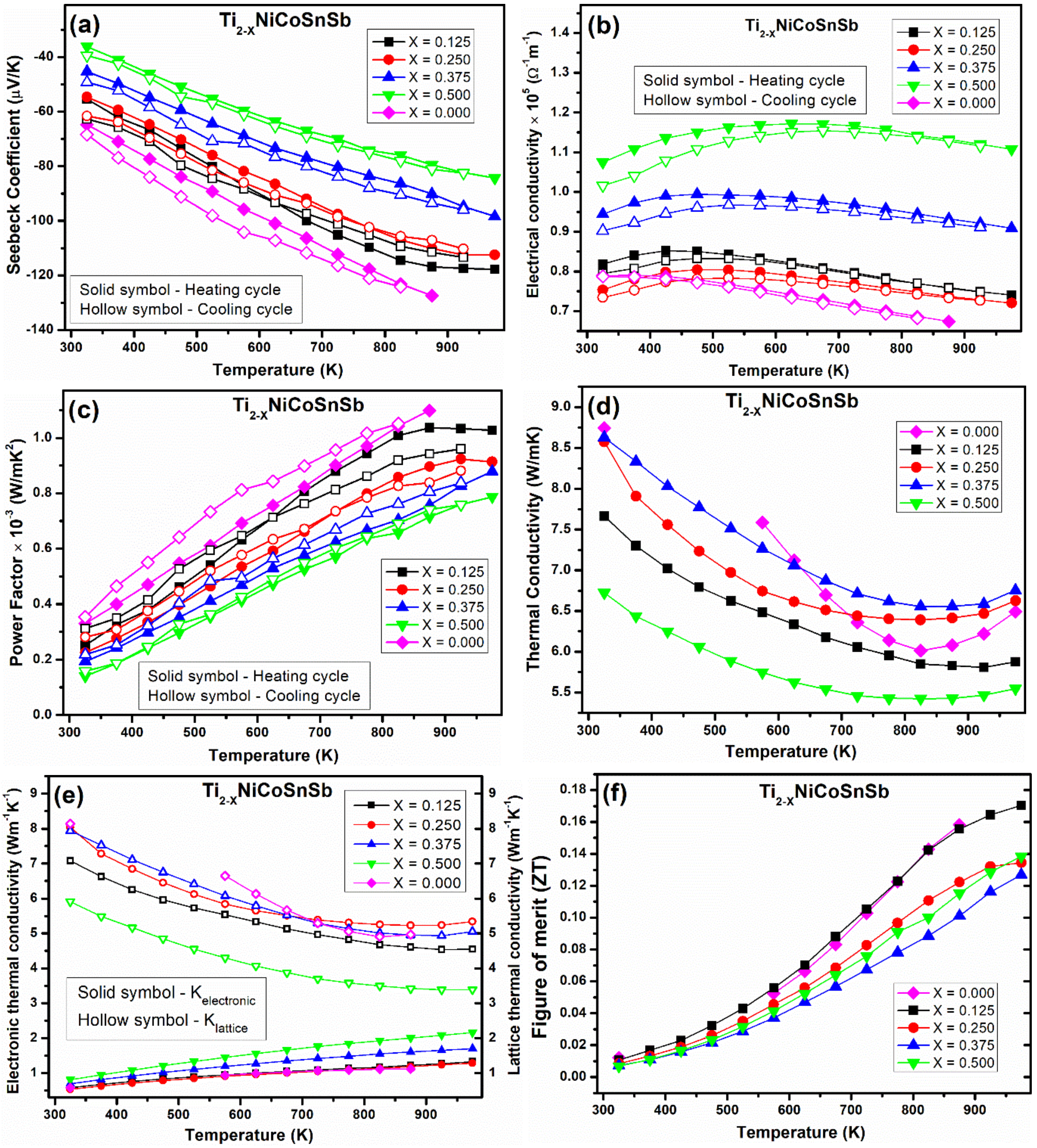

Fig. 8. Thermoelectric properties - (a) Seebeck coefficient (*S*) , (b) electrical conductivity (σ), (c) power factor, (d) thermal conductivity (κ), (e) electronic (solid symbol) and lattice (hollow symbol) thermal conductivity and (f) figure of merit with respect to temperature for $Ti_{2-x}NiCoSnSb$ (X = 0.125 (black), 0.250 (red), 0.375 (blue) and 0.500 (green)) compared with $Ti_2NiCoSnSb$ (extracted from [28]) in magenta.

Considering the κ trend across the temperature range, Figure 8f shows that the x = 0.125 sample had higher *ZT* than the x = 0.000 sample until 773 K. The x = 0.125 sample had a maximum overall *ZT* of 0.171 at 973 K and *ZT* of 0.158 at 873 K, which is again comparable to the maximum *ZT* of 0.16 in the x = 0.000 sample at 873 K [28]. The power factor declined proportionately with a decrease of Ti concentration owing to a rise in the metallic NiSn-rich phase. But the x = 0.500 sample, owing to its lower κ value, had a *ZT* value between that of the x = 0.250 and x = 0.375 samples. The *ZT* is higher than that of TiCoSb (~ 0.016 at 873 K) [16] without any additional annealing for obtaining phase purity, but this value is lower than that of TiNiSn (~ 0.32 at 873 K) [36]. Hence, while there was a marginal enhancement in the figure of merit through lower thermal conductivity, it was counterweighed by the lowering of power factor for lower Ti content. The maximum *ZT* may be enhanced by the introduction of dopants in addition to lowering the Ti content in $Ti_2NiCoSnSb$ to tune the carrier concentration and enhance the power factor.

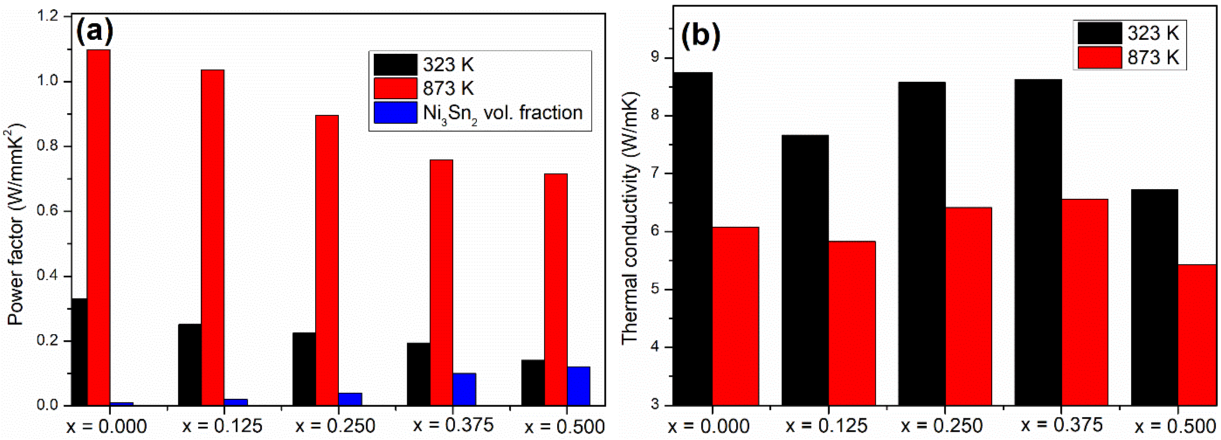

Fig. 9. (a) Variation of power factor and Ni_3Sn_2 phase content with composition and (b) variation of thermal conductivity with composition.

3.3. First principles analysis

The DFT analysis of $Ti_2NiCoSnSb$ revealed a small positive enthalpy difference as compared to the parent HH TiNiSn and TiCoSb, which indicated phase separation in the alloy [29]. Apart from the 2 HH phases in the matrix, owing to the formation of Ti oxycarbides, the Ni_3Sn_2 phase was observed, as rationalized by the mechanochemical reaction.

DFT analysis with similar parameters for the x = 0.000 sample was used for first-principles calculations in the x = 0.500 sample with 8 vacancy sites in the 96-atom supercell simulated from Monte Carlo calculations in ATAT. First-principles calculations of the competing secondary phases were carried out and the final enthalpy per atom is depicted in Figure 10a and in Table S5 of the Supporting information. The calculations were found to be in close agreement with the data in Materials Project [48], as shown in Table S5 of the Supporting information. For Ti content decreasing from the x = 0.000 to the x = 0.500 sample, the HH phase enthalpy increased from -6.57 to -5.69 eV/atom. Hence, further phase separation was observed with the matrix containing a TiCoSb HH phase content (enthalpy of -6.96 eV/atom), the secondary phase fraction increased.

The HH phase fraction decreased by ~12 volume % from x = 0.000 to x = 0.500 sample. Even for a VEC value of 17 in the x = 0.500 sample, the FH phase was detected owing to its lower enthalpy (-6.09 eV/atom) compared to that of $Ti_{1.5}NiCoSnSb$. Furthermore, Ni_3Sn_2 with an enthalpy (-5.1 eV/atom) closer to that of $Ti_{1.5}NiCoSnSb$ was also observed, which could be due to the matrix being TiCoSb rich and the fact that there is insufficient Ti to form the TiNiSn phase.

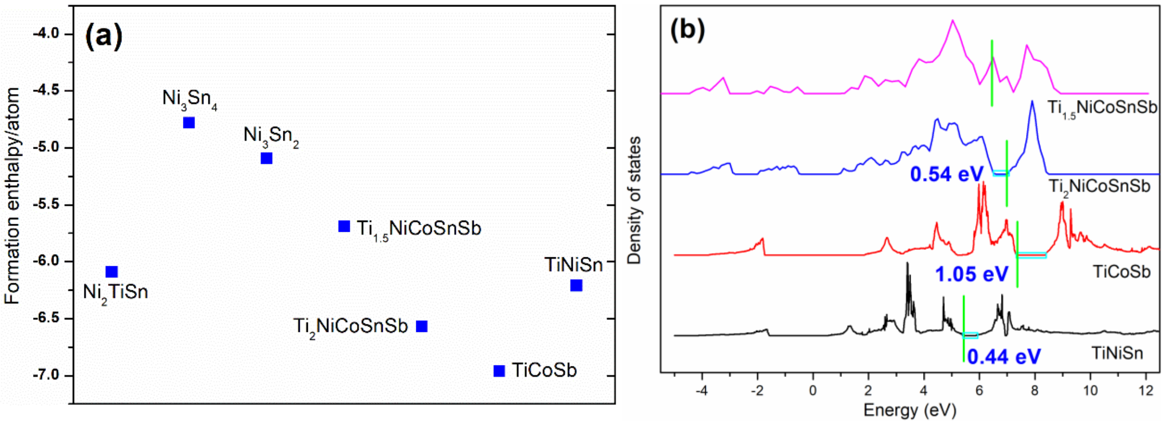

Fig. 10. (a) Formation enthalpy of selective compositions, (b) density of states comparison of $Ti_2NiCoSnSb$ (reported in [29]) and $Ti_{1.5}NiCoSnSb$ with their parent HH alloys.

It has been observed that the Fermi level and band gap lie between that of TiNiSn and TiCoSb for $Ti_2NiCoSnSb$ [29]. The DOS of $Ti_2NiCoSnSb$ (Figure 10b) is a superimposition of that of TiNiSn and TiCoSb, with the convergence of DOS of TiNiSn and TiCoSb discernible in the DOS of $Ti_2NiCoSnSb$. This, in addition to the flattening of the DOS near the fermi level [49], leads to a higher Seebeck coefficient of $Ti_2NiCoSnSb$ as compared to TiNiSn [28, 36]. The narrowing of the band gap as compared to TiCoSb leads to higher electrical conductivity in $Ti_2NiCoSnSb$ [16, 45]. But, in the case of $Ti_{1.5}NiCoSnSb$, no band gap was observed (Figure 10b, Figure S3 of the supporting information). The Fermi level of $Ti_{1.5}NiCoSnSb$, as compared to $Ti_2NiCoSnSb$ shifted to lower energy, indicating p-type doping, which is consistent with the lowering of VEC from 18 to 17. Experimentally though, the $Ti_{1.5}NiCoSnSb$ HH phase was not obtained. Instead, $Ti_2NiCoSnSb$ double HH (TiCoSb-rich) phase with Ni_3Sn_2 metallic phase was found. The metallic phase lowered the Goldsmid-Sharp [44] thermal band gap from 0.23 eV in $Ti_2NiCoSnSb$ to 0.14 eV in $Ti_{1.5}NiCoSnSb$ as evident from the decreasing Seebeck coefficient for lower Ti content samples. Hence, considering the phase separation and the evolution of the FH and the Ni_3Sn_2 phases, the actual band structure might vary from the ground state DFT prediction. This could lead to deviation in obtained transport properties as compared to that calculated using first principles. Further investigation into the phase evolution at various temperature scales and their impact on the transport properties could help in optimizing the composition for obtaining the highest power factor and figure of merit.

4. Conclusions

The relative ease of formation of the majority phase in the entropy-stabilized HH HEA $Ti_2NiCoSnSb$ has been previously reported [28]. The Ti content was lowered in $Ti_{2-x}NiCoSnSb$ alloys to study the effect of the second phase on the TE properties of the HEA. Ti-rich and FH phases were observed in all the samples. Ni-based intermetallic (Ni_3Sn_2, Ni_3Sn_4) phases increased on lowering of Ti content owing to insufficient Ti concentration to form the TiNiSn phase. This improved the electrical conductivity and lowered κ_l at the expense of the S value. First-principles calculations revealed the formation enthalpy of $Ti_{1.5}NiCoSnSb$ to be higher than that of $Ti_2NiCoSnSb$ and full Heusler (FH) $TiNi_2Sn$ and close to that of Ni_3Sn_2. As such, the FH and Ni_3Sn_2 phases could be observed even in these alloys. $Ti_{1.5}NiCoSnSb$ yielded lower thermal conductivity of 5.4 W/mK compared to 6.1 W/mK of $Ti_2NiCoSnSb$ owing to phonon scattering at the HH/Ni_3Sn_2 interfaces. The maximum ZT of 0.171 at 973 K for $Ti_{1.875}NiCoSnSb$ is marginally higher than that of $Ti_2NiCoSnSb$ (0.16 at 873 K). It is higher than that of TiCoSb (~ 0.01 at 873 K) [16] without any additional annealing for obtaining phase purity. This value is lower than that of TiNiSn (~ 0.32 at 873 K) [36]. Further compositional tuning is hence necessary to enhance the power factor and ZT in these alloys.

Acknowledgement

We are thankful to the Department of Metallurgical and Materials Engineering, Indian Institute of Technology Madras for their facilities and technical support that aided the material synthesis and characterization. We are also grateful to the HPCE, IIT Madras for their supercomputing facility (Aqua) that enabled the first-principles studies performed in this study. This work is financially sponsored by AME Programmatic Fund by the Agency for Science, Technology and Research, Singapore under Grant No. A1898b0043 and A18B1b0061.

Notes: Data availability and supporting data

The detailed parameters used for DFT calculations, and the csv files of the raw data are available on request to the corresponding author. Data on densities, EDS analysis, lattice parameters and enthalpies are given in the Supporting data file.

Author contributions

Soumya Ranjan Mishra and Anirudha Karati - Conceptualization, Data curation, Formal analysis, Investigation, Methodology, and Writing – original draft

Sanyukta Ghosh – Investigation, Writing – review and editing.

Ramesh Chandra Mallik, Rajashekhara Shabadi and P Sankara Rama Krishnan

- Formal analysis and Investigation

Satyesh Kumar Yadav – Formal analysis, Writing – review and editing.

R.V. Ramanujan and B.S. Murty –Project administration, Formal analysis, Writing – review, and editing, and Supervision.

Conflict of interest declaration

The authors declare **no competing financial or personal interests** concerning the work reported in this manuscript to the best of their knowledge.

Ethical approval

Not applicable.

References

1. Beretta D, Neophytou N, Hodges JM, et al (2019) Thermoelectrics: From history, a window to the future. Mater Sci Eng R Reports 138:210–255. https://doi.org/10.1016/j.mser.2018.09.001
2. Yurddaskal M, Yurddaskal M, Yilmaz O, Gultekin S (2021) Thermoelectric Films for Electricity Generation. In: Inorganic and Organic Thin Films. pp 299–339
3. Hu B, Shi XL, Zou J, Chen ZG (2022) Thermoelectrics for medical applications: Progress, challenges, and perspectives. Chem Eng J 437:135268. https://doi.org/10.1016/j.cej.2022.135268
4. Ochieng AO, Megahed TF, Ookawara S, Hassan H (2022) Comprehensive review in waste heat recovery in different thermal energy-consuming processes using thermoelectric generators for electrical power generation. Process Saf Environ Prot 162:134–154. https://doi.org/10.1016/j.psep.2022.03.070
5. Al-Tahaineh H, AlEssa AHM (2022) A hybrid TEG/evacuated tube solar collectors for electric power generation and space heating. J Eng Appl Sci 69:1–15. https://doi.org/10.1186/s44147-021-00065-1
6. Farrar-Foley, Nicholas; Rongione, Nicholas; Wu, Huan; Lavine, Adrienne S.; Hu Y (2021) Total solar spectrum energy converter with integrated photovoltaics, thermoelectrics, and thermal energy storage: System modeling and design. Int J Energy Res 46:5731–5744. https://doi.org/10.1002/er.7518
7. Freer R, Powell A V. (2020) Realising the potential of thermoelectric technology: A Roadmap. J Mater Chem C 8:441–463. https://doi.org/10.1039/c9tc05710b
8. Vedernikov M V., Iordanishvili EK (1998) A . F . Ioffe and Origin of Modern

Semiconductor Thermoelectric Energy Conversion. Int Conf Thermoelectr 17:37–42

9. Fitriani, Ovik R, Long BD, et al (2016) A review on nanostructures of high-temperature thermoelectric materials for waste heat recovery. Renew Sustain Energy Rev 64:635–659. https://doi.org/10.1016/j.rser.2016.06.035
10. Baday C, Yurddaskal M, Ozgul M, Zor M (2017) Production , characterization and optimization of thermoelectric module and investigation of doping effects on thermoelectric performances. J Mater Sci Mater Electron 28:17468–17481. https://doi.org/10.1007/s10854-017-7681-0
11. Sootsman JR, Chung DY, Kanatzidis MG (2009) New and old concepts in thermoelectric materials. Angew Chemie - Int Ed 48:8616–8639. https://doi.org/10.1002/anie.200900598
12. Poon SJ (2019) Half Heusler compounds: Promising materials for mid-to-high temperature thermoelectric conversion. J Phys D Appl Phys 52:493001. https://doi.org/10.1088/1361-6463/ab3d71
13. Liu R, Xing Y, Liao J, et al (2022) Thermal-inert and ohmic-contact interface for high performance half-Heusler based thermoelectric generator. Nat Commun 13:7738. https://doi.org/10.1038/s41467-022-35290-6
14. Quinn RJ, Bos JWG (2021) Advances in half-Heusler alloys for thermoelectric power generation. Mater Adv 2:6246–6266. https://doi.org/10.1039/d1ma00707f
15. Chen K, Zhang R, Bos JWG, Reece MJ (2022) Synthesis and thermoelectric properties of high-entropy half-Heusler $MFe_{1-x}Co_xSb$ (M = equimolar Ti, Zr, Hf, V, Nb, Ta). J Alloys Compd 892:162045. https://doi.org/10.1016/j.jallcom.2021.162045
16. Sekimoto T, Kurosaki K, Muta H, Yamanaka S (2006) Thermoelectric properties of Sn-doped TiCoSb half-Heusler compounds. J Alloys Compd 407:326–329. https://doi.org/10.1016/j.jallcom.2005.06.036
17. Wang Q, Xie X, Li S, et al (2021) Enhanced thermoelectric performance in Ti(Fe, Co, Ni)Sb pseudo-ternary Half-Heusler alloys. J Mater 7:756–765. https://doi.org/10.1016/j.jmat.2020.12.015
18. Karati A, Murty BS (2017) Synthesis of nanocrystalline half-Heusler TiNiSn by mechanically activated annealing. Mater Lett 205:114–117. https://doi.org/10.1016/j.matlet.2017.06.068
19. Bahrami A, Ying P, Wolff U, et al (2021) Reduced Lattice Thermal Conductivity for Half-Heusler ZrNiSn through Cryogenic Mechanical Alloying. ACS Appl Mater Interfaces 13:38561–38568. https://doi.org/10.1021/acsami.1c05639
20. Tillard M, Berche A, Jund P (2018) Synthesis of pure NiTiSn by mechanical alloying: An investigation of the optimal experimental conditions supported by first principles calculations. Metals (Basel) 8:835. https://doi.org/10.3390/met8100835
21. Park G, Lee HS, Yi S (2022) Effects of Annealing on the Microstructure and Thermoelectric Properties of Half-Heusler MNiSn (M = Ti, Zr, Hf). J Electron Mater 51:3485–3494. https://doi.org/10.1007/s11664-022-09627-2
22. Chen LD, Huang XY, Zhou M, et al (2006) The high temperature thermoelectric performances of $Zr_{0.5}Hf_{0.5}Ni_{0.8}Pd_{0.2}Sn_{0.99}Sb_{0.01}$ alloy with nanophase inclusions. J Appl Phys 99:064305. https://doi.org/10.1063/1.2180432
23. Makongo JPA, Misra DK, Zhou X, et al (2011) Simultaneous large enhancements in thermopower and electrical conductivity of bulk nanostructured half-Heusler alloys. J Am Chem Soc 133:18843–18852. https://doi.org/10.1021/ja206491j
24. Yang X, Wang Y, Min R, et al (2022) Enhancement in thermoelectric properties of ZrNiSn-based alloys by Ta doping and Hf substitution. Acta Mater 233:117976. https://doi.org/10.1016/j.actamat.2022.117976
25. Hasan MA Al, Wang J, Shin S, et al (2021) Effects of aluminum content on

thermoelectric performance of $Al_xCoCrFeNi$ high-entropy alloys. J Alloys Compd 883:160811. https://doi.org/10.1016/j.jallcom.2021.160811

26. Ren W, Shi X, Wang Z, Ren Z (2022) Crystallographic design for half-Heuslers with low lattice thermal conductivity. Mater Today Phys 25:100704. https://doi.org/10.1016/j.mtphys.2022.100704
27. Graf T, Klaer P, Barth J, et al (2010) Phase separation in the quaternary Heusler compound $CoTi_{(1-x)}Mn_xSb$ - A reduction in the thermal conductivity for thermoelectric applications. Scr Mater 63:1216–1219. https://doi.org/10.1016/j.scriptamat.2010.08.039
28. Karati A, Nagini M, Ghosh S, et al (2019) $Ti_2NiCoSnSb$ - a new half-Heusler type high-entropy alloy showing simultaneous increase in Seebeck coefficient and electrical conductivity for thermoelectric applications. Sci Rep 9:5331. https://doi.org/10.1038/s41598-019-41818-6
29. Karati A, Mishra SR, Ghosh S, et al (2022) Thermoelectric properties of a high entropy half-Heusler alloy processed by a fast powder metallurgy route. J Alloys Compd 924:166108. https://doi.org/10.1016/j.jallcom.2022.166108
30. Hoch M, Vardi J (1963) Thermal conductivity of TiC. J Am Ceram Soc 46:245
31. He R, Huang L, Wang Y, et al (2016) Enhanced thermoelectric properties of n-type NbCoSn half-Heusler by improving phase purity. APL Mater 4:104804. https://doi.org/10.1063/1.4952994
32. Ferluccio DA, Smith RI, Buckman J, Bos JWG (2018) Impact of Nb vacancies and p-type doping of the NbCoSn-NbCoSb half-Heusler thermoelectrics. Phys Chem Chem Phys 20:3979–3987. https://doi.org/10.1039/c7cp07521a
33. Xia K, Liu Y, Anand S, et al (2018) Enhanced Thermoelectric Performance in 18-Electron $Nb_{0.8}CoSb$ Half-Heusler Compound with Intrinsic Nb Vacancies. Adv Funct Mater 28:1–7. https://doi.org/10.1002/adfm.201705845
34. Ferluccio DA, Halpin JE, Macintosh KL, et al (2019) Low thermal conductivity and promising thermoelectric performance in A_XCoSb (A = V, Nb or Ta) half-Heuslers with inherent vacancies. J Mater Chem C 7:6539–6547. https://doi.org/10.1039/c9tc00743a
35. Huang L, Liu T, Huang A, et al (2021) Enhanced thermoelectric performance of nominal 19-electron half-Heusler compound NbCoSb with intrinsic Nb and Sb vacancies. Mater Today Phys 20:100450. https://doi.org/10.1016/j.mtphys.2021.100450
36. Douglas JE, Birkel CS, Verma N, et al (2014) Phase stability and property evolution of biphasic Ti-Ni-Sn alloys for use in thermoelectric applications. J Appl Phys 115:0–11. https://doi.org/10.1063/1.4862955
37. Tippireddy S, Chetty R, Naik MH, et al (2018) Electronic and Thermoelectric Properties of Transition Metal Substituted Tetrahedrites. J Phys Chem C 122:8735–8749. https://doi.org/10.1021/acs.jpcc.7b12214
38. Van De Walle A, Tiwary P, De Jong M, et al (2013) Efficient stochastic generation of special quasirandom structures. calphad Comput coupling for phase diagrams Thermochem 42:13–18. https://doi.org/10.1016/j.calphad.2013.06.006
39. Kohn W, Sham LJ (1965) Self-Consistent Equations Including Exchange and Correlation Effects*. Phys Rev 140:A1133–A1138
40. Perdew JP, Burke K, Ernzerhof M (1996) Generalized gradient approximation made simple. Phys Rev Lett 77:3865–3868. https://doi.org/10.1103/PhysRevLett.77.3865
41. Hazama H, Matsubara M, Asahi R, Takeuchi T (2011) Improvement of thermoelectric properties for half-Heusler TiNiSn by interstitial Ni defects. J Appl Phys 110:063710. https://doi.org/10.1063/1.3633518
42. Gürth M, Grytsiv A, Vrestal J, et al (2015) On the constitution and thermodynamic modelling of the system Ti-Ni-Sn. RSC Adv 5:92270–92291.

https://doi.org/10.1039/c5ra16074j

43. Gharleghi A, Hung RH, Yang ZR, et al (2018) Enhanced thermoelectric properties of hydrothermally synthesized $Bi_{0.88-X}Zn_XSb_{0.12}$ nanoalloys below the semiconductor-semimetal transition temperature. RSC Adv 8:20764–20772. https://doi.org/10.1039/c8ra03858a
44. Goldsmid HJ, Sharp JW (1999) Estimation of the thermal band gap of a semiconductor from Seebeck measurements. J Electron Mater 28:869–872. https://doi.org/10.1007/s11664-999-0211-y
45. Chauhan NS, Bhattacharjee D, Maiti T, et al (2022) Low Lattice Thermal Conductivity in a Wider Temperature Range for Biphasic-Quaternary (Ti,V)CoSb Half-Heusler Alloys. ACS Appl Mater Interfaces 14:54736–54747. https://doi.org/10.1021/acsami.2c16595
46. Yang X, Liu D, Li J, et al (2021) Top-down method to fabricate TiNi1+xSn half-Heusler alloy with high thermoelectric performance. J Mater Sci Technol 87:39–45. https://doi.org/10.1016/j.jmst.2021.01.052
47. Karati A, Ghosh S, Mallik RC, et al (2022) Effect of Processing Routes on the Microstructure and Thermoelectric Properties of Half-Heusler $TiFe_{0.5}Ni_{0.5}Sb_{1-x}Sn_x$ (x = 0, 0.05, 0.1, 0.2) Alloys. J Mater Eng Perform 31:305–317. https://doi.org/10.1007/s11665-021-06207-z
48. Jain A, Ong SP, Hautier G, et al (2013) Commentary: The materials project: A materials genome approach to accelerating materials innovation. APL Mater 1:011002. https://doi.org/10.1063/1.4812323
49. Jia N, Cao J, Yi X, et al (2021) Thermoelectric materials and transport physics. Mater Today Phys 21:100519. https://doi.org/10.1016/j.mtphys.2021.100519